Zhao *et al. Biochar* (2026) 8:20
https://doi.org/10.1007/s42773-025-00541-4

Biochar

ORIGINAL RESEARCH Open Access

Coffee grounds derived porous nitrogen-rich biochar as a metal-free catalyst for efficient selective oxidation of hydrogen sulfide to sulfur

Fei Zhao[1†], Zibin Pan[1†], Fang Wang[1], Suo Cui[1], Rui Cao[1], Jiayu Feng[1*], Ping Ning[2*] and Lijuan Jia[1*]

Abstract

The development of metal-free catalysts for efficient selective catalytic oxidation of hydrogen sulfide (H_2S-SCO) to elemental sulfur represents a sustainable solution for toxic gas purification. Herein, we synthesized a regenerable metal-free catalyst through facile activation and pyrolysis of coffee grounds. The optimized catalyst demonstrated exceptional H_2S-SCO performance at 180 ℃, achieving > 99% H_2S conversion with near-perfect sulfur selectivity (~ 100%) while maintaining remarkable stability under humid conditions and high CO_2 concentrations. These superior properties originate from the synergistic effects of elevated nitrogen doping (17.33 at.%), abundant defect edge sites, and hierarchical porosity. Density functional theory (DFT) calculations revealed that carbon atoms adjacent to pyridine-N configurations serve as dual-active sites, facilitating H_2S adsorption/dissociation and O_2 activation through optimized electron redistribution. A plausible reaction mechanism was established based on experimental and theoretical analyses. This work provides fundamental insights into designing cost-effective, biomass-derived carbon catalysts for industrial gas purification while addressing agricultural waste valorization.

Highlights

- Sustainable metal-free catalyst derived from coffee grounds
- Unparalleled catalytic performance, industrial scalability, and environmental impact
- Synergistic active sites via nitrogen engineering, and mechanistic clarity for rational catalyst design

Keywords H_2S, Biochar, Catalytic oxidation, Coffee grounds

[†]Fei Zhao and Zibin Pan have contributed equally to this work.

*Correspondence:
Jiayu Feng
FJY_DX3906@163.com
Ping Ning
ningping86@163.com
Lijuan Jia
leegyerkm@163.com

Graphical Abstract

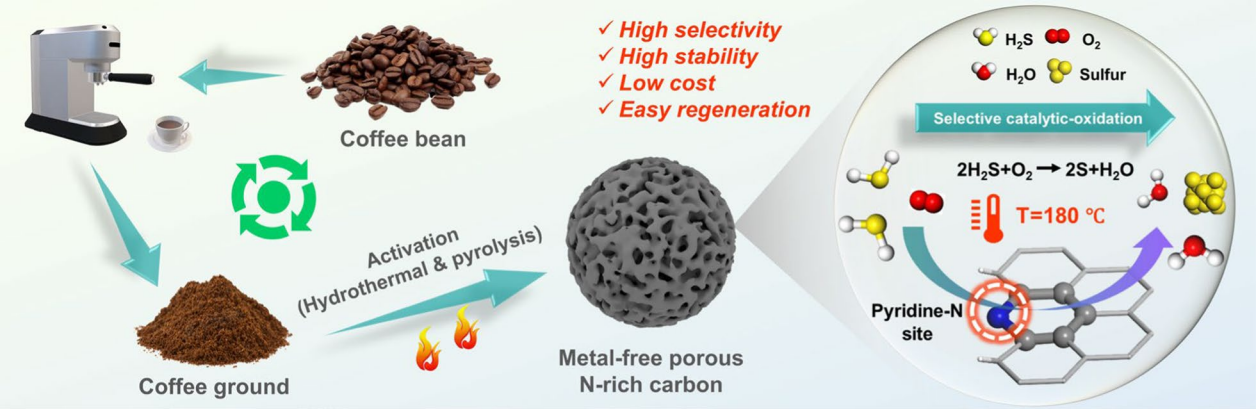

1 Introduction

Hydrogen sulfide (H_2S), a highly toxic and corrosive colorless acidic gaseous pollutant with a distinctive rotten egg odor, represents a significant environmental and industrial challenge (Feng et al. 2023). This hazardous gas primarily derives from various industrial processes, including the iron industry, petroleum cracking, and wastewater treatment facilities (de Rink et al. 2020; Yang et al. 2023). Even trace levels of H_2S (0.01–0.3 ppm) can stimulate the olfactory and nervous systems, and acute exposure to elevated concentrations (> 2000 ppm) triggers immediate respiratory arrest (He et al. 2012; Chan et al. 2022). From an industrial perspective, H_2S can corrode industrial equipment and pipelines and cause poisoning of precious metal or metal oxide catalysts in catalytic processes, significantly escalating operational costs through increased maintenance requirements and process downtime (Khabazipour et al. 2019). More importantly, H_2S is one of the main precursors of acid rain, destroying the balance of the ecosystem. According to relevant environmental regulations, the acceptable limit of H_2S in the environment is 0.02–0.1 ppm (Meng et al. 2013). Hence, appropriate treatment of H_2S-containing waste gas reduces H_2S concentration to avoid environmental and human health hazards and complies with environmental regulations and ecological safety needs.

The primary industrial desulfurization techniques encompass the Claus process, solid adsorption (Martínez-Ahumada et al. 2020), liquid phase absorption (Shah et al. 2017), and catalytic oxidation (Zhang et al. 2015), to name a few. The Clausa process can convert high concentrations of H_2S into elemental sulfur through staged thermal reactions, but due to thermodynamic limitations, 3%– 5% of H_2S remains in effluent gases (Brazhnyk et al. 2007). Solid adsorbents operate simply and offer moderate H_2S capture capacity under ambient conditions. However, they face critical limitations. These include frequent regeneration needs that increase operational expenditures and, more importantly, the generation of spent adsorbents. These spent materials pose risks of secondary environmental contamination, which fundamentally conflicts with circular economy principles. Alternatively, liquid-phase absorption systems enable rapid H_2S sequestration using alkaline or amine-based solvents. Nevertheless, their widespread application is hampered by the creation of sulfur-laden waste streams, which require complex and costly disposal procedures. In contrast, catalytic oxidation presents an overwhelming advantage. This process uses molecular oxygen to selectively convert H_2S to elemental sulfur ($H_2S + 1/2\ O_2 \rightarrow 1/n\ S_n + H_2O$). It is currently regarded as an effective and sustainable strategy for H_2S removal due to its mild operating conditions, thermodynamic completeness, and ecological merit. A key strength of this technology is its high efficiency, being capable of reducing residual H_2S in the off-gas to ultra-low concentrations (< 0.1 ppm) (Xu et al. 2021a, b).

Although H_2S-SCO is a promising strategy, striking a balance between conversion and selectivity remains a great challenge (Phatyenchuen et al. 2018), the key to which lies in the development of high-performance catalysts. The catalysts employed for the H_2S-SCO are classified mainly into metal oxide-based and carbon-based catalysts. So far, various metal oxide-based catalysts, such as Fe_2O_3, CeO_2, and V_2O_5, with high catalytic oxidation activity for H_2S have been widely used for H_2S-SCO (Zheng et al. 2021, 2019). During the desulfurization

reaction using metal oxide-based catalysts, high temperatures and excessive oxygen are required, and the p-orbital of the S atoms and the d-orbital of the metal atoms can overlap heavily to form metal-sulfur covalent bonds, inducing the formation of metal sulfates, which makes sulfur selectivity decline dramatically (Lei et al. 2020). Moreover, due to the small specific surface area, the sulfur products generated during the reaction can easily cover the active sites and accelerate catalyst deactivation (Zheng et al. 2020). Alternatively, the doping of heteroatoms (such as N, P, and S) in biochar substrates significantly alters the surface chemistry and pore structure of metal-free carbon-based catalysts, where doping N heteroatoms can enhance surface polarity, improve electron-donating properties, and provide ample Lewis base sites to improve the ability of the carbon catalyst to catalyze oxidation (Liang et al. 2020; Liu et al. 2020; Wang et al. 2024a, b). Consequently, Xu and co-workers (Xu et al. 2021a, b) prepared honeycomb porous N-doped carbon (NPC), and the sulfur formation rate of NPC700 reached an impressive 496.6 $g_{sulfur}/kg_{cat}/hg_{sulfur}/kg_{cat}/h$, but the desulfurization performance decreased steadily after only 45 h during the stability test. Yang et al. (2020a, b) reported a nitrogen-rich carbon catalyst, and the conversion of H_2S reached 99% at 180 °C, with a sulfur selectivity of 95%. However, the high cost of precursors for synthesizing the catalysts limits their large-scale application. Kan et al. (2019) synthesized a class of N-functionalized ordered mesoporous carbon spheres with a large surface area (> 1200 m^2/g), but, limited by their low nitrogen content, they achieved an optimal sulfur capacity of only 13.4 mmol/g. Generally, the high removal capacity of H_2S relies on a combination of factors, such as the number of basic active sites, the density of structural defects, and the specific surface area. Therefore, there is an urgent need to develop a green, low-cost, and simple strategy for synthesizing carbon materials with a large specific surface area, sufficient structural defects, and high nitrogen content for efficient H_2S-SCO.

Coffee, one of the world's most popular beverages, has a global consumer market. According to the latest statistics, the global coffee plantation area reached 167 million acres in 2021, with a production of about 10.05 million tons, indicating that the coffee industry is developing rapidly. As a result, more than 6 million tons of coffee grounds (CG) are generated globally each year during the production of coffee beverages (Battista et al. 2020). The CG mainly contains a variety of harmful substances, such as caffeine, tannins, and polyphenols (Pagett et al. 2023), which are very harmful to handle in the environment. However, over half of the CG is directly landfilled or incinerated, and a small amount is used as organic fertilizer. With the prolongation of time, they will decompose and release a large amount of CH_4 and CO_2, which will have an immeasurable impact on the environment (Franca et al. 2022). Fortunately, dried CG contains about 70 wt.% carbon, making it an excellent precursor for activated carbon (Kourmentza et al. 2018). Therefore, converting CG into high-value carbon materials effectively solves the problems of environmental pollution and resource waste caused by the direct disposal of coffee grounds and ultimately realizes a low-carbon, green circular economy. Kim et al. (Kim et al. 2020) synthesized microporous carbon adsorbents with a specific surface area of up to 2337 m^2/g for CO_2 adsorption by solid-state K_2CO_3 activation using coffee grounds as raw material. These findings suggest that CG is a potentially excellent carbon source for synthesizing nitrogen-rich carbon catalysts. As far as we know, there exists no report on synthesizing nitrogen-rich carbon catalysts using the CG as a carbon source for the H_2S-SCO process.

Motivated by the above, this study presents a novel metal-free, nitrogen-enriched carbon catalyst fabricated through a sustainable two-step synthesis strategy involving hydrothermal carbonization of CG followed by pyrolytic activation. The catalyst demonstrates exceptional catalytic performance in H_2S-SCO, achieving 100% H_2S conversion efficiency while maintaining remarkable stability under harsh operational conditions, including extreme CO_2-rich atmospheres (50 vol.%) and high humidity (RH = 80%). Furthermore, we employed advanced characterization techniques and DFT calculations to systematically elucidate the adsorption-dissociation of H_2S molecules, the activation of O_2 molecules, and the formation of elemental sulfur, thereby proposing the reaction mechanism of H_2S-SCO over the catalyst. This work establishes a novel paradigm for simultaneous agricultural waste valorization and toxic gas purification, offering fundamental insights into metal-free catalytic systems that align with global green chemistry initiatives.

2 Experimental section

2.1 Preparation of catalysts

The catalyst synthesis procedure is illustrated in Fig. 1a. Specific steps are as follows: hydrothermal carbonization (180 °C, 12 h) converted raw biomass into hydrothermally carbonized coffee grounds (HCG), eliminating organic impurities, including lignin and microbial contaminants. The HCG was combined with melamine cyanurate (MCA) and KOH through 1 h of ultrasonication-assisted mixing, followed by overnight drying at 105 °C. Pyrolysis was conducted under N_2 flow at different temperatures for 2 h. The carbonized product underwent repeated deionized water washing until it reached a neutral pH to yield nitrogen-enriched catalysts designated as CGNrC-T (T = pyrolysis

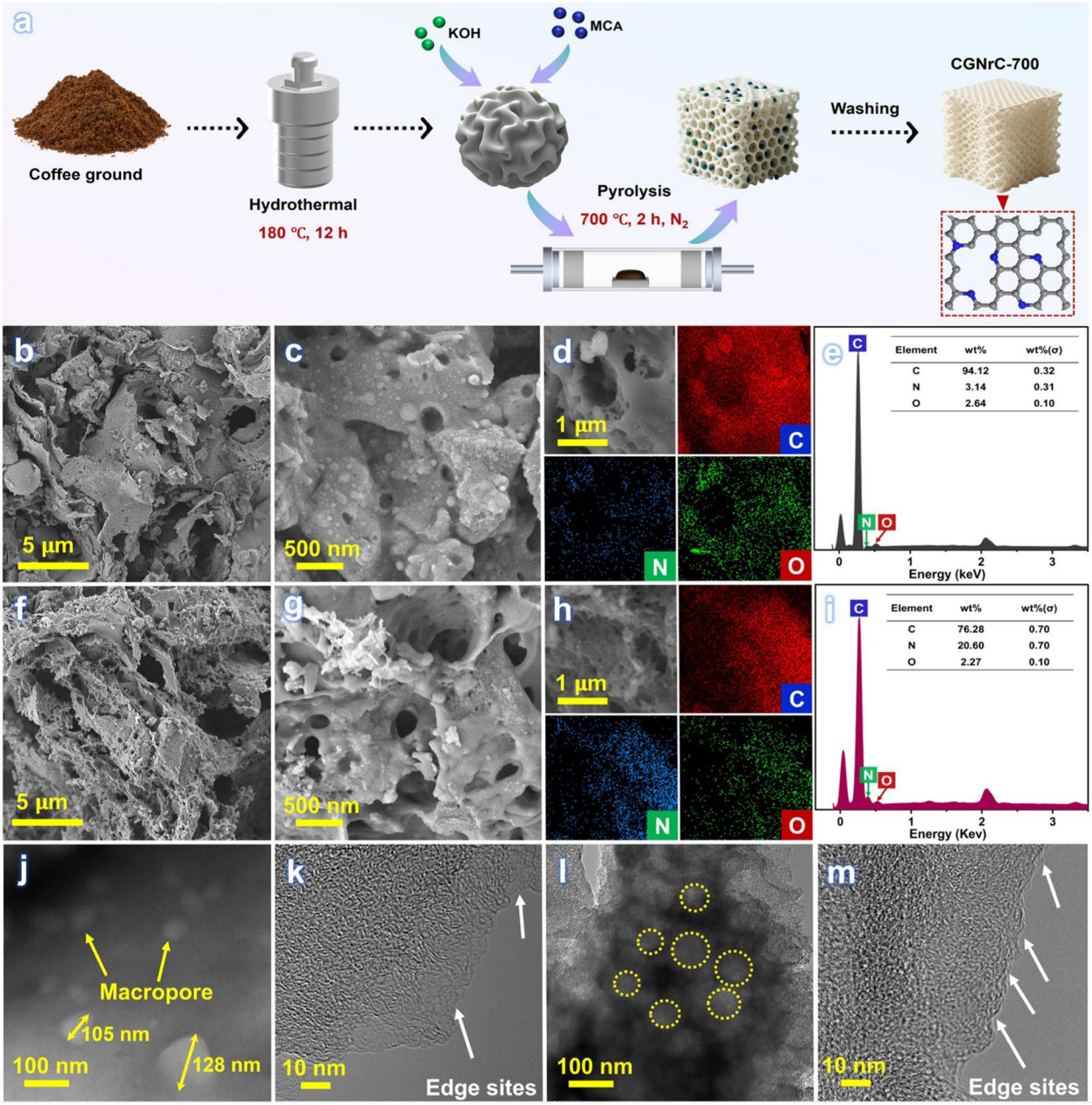

Fig. 1 **a** Diagram of the nitrogen-rich carbon catalyst preparation procedure. **b**, **c** and **f**, **g** SEM images of CGC-700, CGNrC-700. **d**, **h** EDS mapping image showing the elemental distribution of C, N, and O of CGC-700 and CGNrC-700. **e**, **i** Energy spectrum of CGC-700, CGNrC-700. **j**, **l** TEM images, and **l**, **m** HR-TEM images of CGC-700, CGNrC-700

temperature). A comparative sample (CGC-700) was prepared through direct pyrolysis of HCG at 700 °C for 2 h without pretreatment. This hierarchical approach enabled controlled nitrogen doping while maintaining a porous carbon architecture through coordinated chemical activation and thermal decomposition. Part of the detailed procedure is provided in Appendix S1.

2.2 Characterization methods

The structural evolution and chemical composition of the samples were characterized by methods such as

thermogravimetric analysis (TGA), X-ray diffraction (XRD), Raman spectroscopy, Fourier transform infrared (FT-IR), and X-ray photoelectron spectroscopy (XPS). The surface morphology and elemental composition of samples were investigated by scanning electron microscopy (SEM), and the microstructure of the samples was observed by transmission electron microscopy (TEM). The pore structure of the carbon materials was characterized using nitrogen (N_2) adsorption–desorption isotherms. The CO_2 temperature-programmed desorption (CO_2-TPD) and the O_2 temperature-programmed desorption (O_2-TPD) were used to probe the strength and number of basic sites and the ability of carbon materials to adsorb and release oxygen. More detailed descriptions are provided in Appendix S2.

2.3 H_2S-SCO activity test system

Figure S1 presents a diagram of the desulfurization reaction system. The catalyst was placed into a quartz reaction tube with an inner diameter of 6 mm, which was subsequently placed in a small tube furnace reactor. The feed gas at a total flow rate of 100 mL/min (comprising 0.1 vol.% H_2S, 0.05 vol.% O_2, and balance N_2) was passed through a fixed-bed reactor containing 0.1 g of catalyst in a fixed-bed reactor. The reaction temperature range was set at 60–210 ℃, and the concentrations of H_2S at the outlet were monitored by a fixed detector (DR70C-H_2S). The concentration of the product SO_2 in the exhaust gas was analyzed and detected using a fixed sulfur dioxide detector (DR70C-SO_2). The point at which the outlet concentration of H_2S reaches 0.01 vol.% is defined as the breakthrough time. A more detailed description of the H_2S-SCO process is given in Appendix S3. (The experimental results of the catalytic oxidation performance test of all the samples covered in the paper were repeated twice.)

Furthermore, H_2S conversion (X_{H_2S}), sulfur selectivity (S_S), and sulfur yield (Y_S) were calculated according to the following Eqs. (1)-(3).

$$X_{H_2S}\,(\%) = \frac{[H_2S]_{in} - [H_2S]_{out}}{[H_2S]_{in}} \times 100 \quad (1)$$

$$S_S\,(\%) = \frac{[H_2S]_{in} - [H_2S]_{out} - [SO_2]_{out}}{[H_2S]_{in} - [H_2S]_{out}} \times 100 \quad (2)$$

$$Y_S = X_{H_2S} S_S \quad (3)$$

where $[H_2S]_{in}$ and $[H_2S]_{out}$ denote the concentrations of H_2S and SO_2 in the inlet gas and outlet gas (ppm), respectively. $[SO_2]_{out}$ is the outlet concentration of SO_2.

2.4 Theoretical computational methods

All density functional theory (DFT) calculations involved in this paper were performed using Gaussian 16.0 and Gaussian View software, and all molecular structures were optimized using the B3LYP method (Pan et al. 2023). A model of monolayer graphene containing defects and nitrogen doping was constructed using monolayer graphene with all atoms fully relaxed. Subsequently, the electrostatic surface potential (ESP) of the nitrogen-rich carbon materials was calculated. The difference between the lowest unoccupied molecular orbital (LUMO) and the highest occupied molecular orbital (HOMO) is known as the energy gap (E_g), and the adsorption energies (E_{ads}) of H_2S and O_2 were evaluated according to the following equation:

$$E_{ads} = E_{slab+A} - E_{slab} - E_A \quad (4)$$

$$E_g = \left| E_{(LUMO)} E_{(HOMO)} \right| \quad (5)$$

where E_{slab+A}, E_{slab}, and E_A are the total energy after adsorption of the molecules, the energy of the pure N-doped biomass carbon slab, and the total energy of the isolated H_2S and O_2 molecules, respectively. The relevant details are provided in Appendix S4.

3 Results and discussion

3.1 Characterization of catalysts

SEM analysis revealed negligible porosity in CGC-700 (Fig. 1b and c), and CGNrC-700 has a three-dimensional hierarchical porous structure similar to a cavern (Fig. 1f and g). Temperature-dependent pore evolution analysis demonstrated that the pyrolysis temperature affects the pore structure of the catalysts. Limited micropore formation occurred at 500 °C (Fig. S2a), attributed to the underutilized etching effect of KOH at low temperatures. Progressive thermal activation at 900 °C induced well-developed hierarchical pore structures (Fig. S2b). Elemental analysis quantified remarkable nitrogen enrichment (3.14–20.60 wt.%) post-MCA doping (Fig. 1e and i), confirming effective heteroatom incorporation. However, higher carbonization temperatures may hinder the anchoring of nitrogen substances in the carbon skeleton, as shown in the EDS spectral analysis (Fig. S3a and b), where nitrogen content decreased from 31.37 wt.% to 4.97 wt.%, establishing 700 °C as the thermal optimization threshold. Meanwhile, the elemental mapping confirmed homogenous dispersion of C, N, and O elements on the carbon matrix surface across all specimens (Figs. 1d, h, and 2f and S2). TEM characterization disclosed that only a few macropores larger than 100 nm were observed in CGC-700, while CGNrC-700 possesses an interconnected pore channel constructed by many 2D

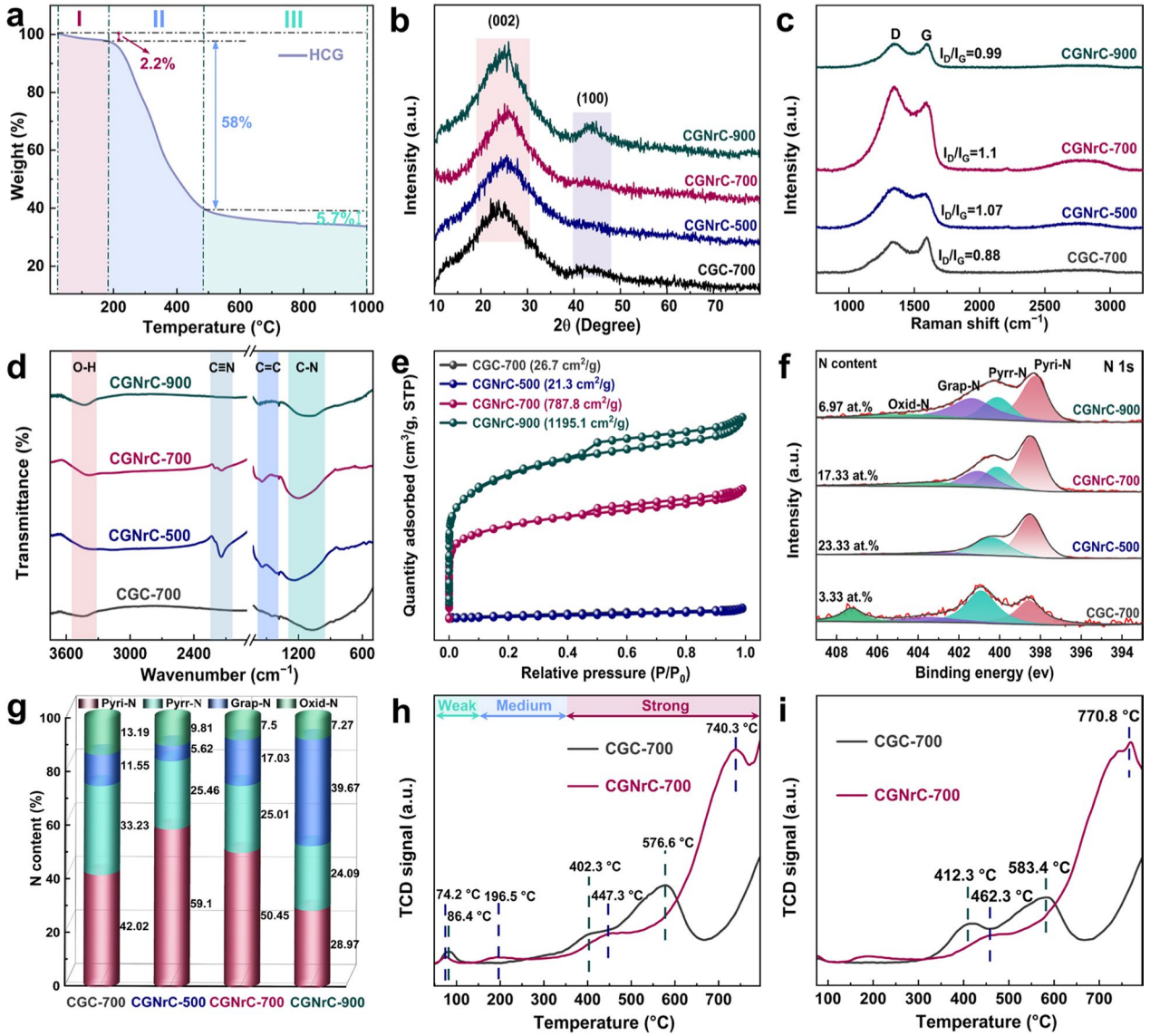

Fig. 2 **a** TG curve spectra of HCG in the 0 ~ 1000 °C temperature range. **b** XRD patterns, **c** Raman spectra, **d** N_2 adsorption–desorption isotherms, **e** FT-IR spectra, **f** High-resolution N 1 s XPS spectra, and **g** Nitrogen content of different nitrogen species of all samples. **h** CO_2-TPD and **i** O_2-TPD profiles of CGC-700 and CGNrC-700

ultrathin nanosheets stacked together (Fig. 1j and l). HR-TEM analysis identified abundant topological defects and edge sites favoring active site exposure (Fig. 1k and m).

TGA under a nitrogen atmosphere (20 mL/min flow rate) systematically characterized the pyrolysis behavior of HCG precursors. As delineated in Fig. 2a, three distinct decomposition regimes were identified, an initial 2.2 ± 0.3% mass decrement (≤ 175 °C) corresponding to the desorption of physical adsorption water, a predominant 58 ± 1.2% mass loss (175–475 °C), attributed to concerted devolatilization of lignocellulosic components in the CG (Laksaci et al. 2017), and a residual 3.8 ± 0.5% mass loss (≥ 475 °C), which is related to the decomposition of the nitrogen component and the formation of graphitic carbon. Presumably, the optimal temperature for forming a stabilized carbon skeleton is above 500 °C.

The crystalline structure evolution and graphitization degree of the samples were systematically investigated through XRD and Raman spectroscopy analyses. As shown in Fig. 2b, all samples exhibited two weak and broad diffraction peaks at approximately 25° and 44°, attributed to the (002) and (100) lattice planes of graphitic carbon, respectively (Liu et al. 2022). Notably, the

enhancement in peak intensity at 44° with elevated pyrolysis temperatures indicates improved graphitic ordering. The observed peak broadening and low diffraction intensity imply substantial structural defects and reduced crystallinity, likely originating from the amorphous carbon matrix that disrupts the long-range ordering of the graphitic framework. Complementary Raman spectra (Fig. 2c) revealed two prominent vibrational modes: the D-band at ~ 1350 cm^{-1} (associated with disordered sp^3 carbon domains) and the G-band at ~ 1580 cm^{-1} (characteristic of ordered sp^2 graphitic structures) (Li et al. 2014). As shown in Table S1, the I_D/I_G ratio decreased with increasing temperature (> 700 °C), indicating thermally induced transformation from amorphous carbon to graphitic domains. CGNrC-700 exhibited the highest I_D/I_G ratio (1.1), correlating with maximal defect density and structural disorder. According to previous reports, these structural imperfections create abundant active sites that are crucial for enhancing the catalytic performance of the catalysts (Yang et al. 2020a, b).

The catalytic performance in H_2S oxidation was influenced by the specific surface area (SSA) and hierarchical pore architecture. According to the IUPAC classification of adsorption isotherm types, as shown in Fig. 1d, CGC-700 and CGNrC-500 exhibited type III isotherms with negligible hysteresis, indicative of non-porous or microporous structures, consistent with their low SSAs (26.7 and 21.3 m^2/g, respectively) (Li et al. 2024). In contrast, CGNrC-700 and CGNrC-900 displayed Type I isotherms with H4-type hysteresis loops, characteristic of micro-mesoporous materials possessing high SSAs of 787.8 and 1195.1 m^2/g, respectively (Cychosz et al. 2018). Pore size distribution analysis (Fig. S4) demonstrated a predominant pore diameter range of 1–10 nm across all samples, with an average pore width of 4.3 nm. As shown in Table S2, the assessment of porosity parameters revealed that CGNrC-700 possesses a hierarchical pore system, combining substantial microporosity (0.42 cm^3/g) with limited mesopore volume (0.04 cm^3/g). This microporous dominance contrasts with the interconnected porous networks observed in SEM/TEM images. FT-IR spectroscopy (Fig. 2e) further elucidated the chemical evolution during pyrolysis. Distinct vibrational bands at 1565 cm^{-1} (C=N stretching) and 2146 cm^{-1} (C≡N stretching) were identified in all samples except CGC-700. These peaks diminished with increasing pyrolysis temperature (> 700 °C) that correlate with the thermal decomposition of nitrogen-containing functional groups. As depicted in Fig. S3, this trend is corroborated by elemental analysis.

XPS was employed to elucidate the chemical speciation and elemental evolution. The wide survey spectra confirmed the coexistence of C, N, and O elements in all samples (Fig. S5). Deconvolution of the C 1 s spectra (Fig. S6a) revealed six distinct components: graphitic carbon (C–C/C=C, ~ 284.8 eV), heteroatom-bonded carbon (C–N/C–O, ~ 285.7 eV), carbonyl groups (C=O, ~ 286.8 eV), carboxyl groups (–COO, ~ 288.4 eV), along with characteristic π-π^* satellite features at ~ 293.0 eV and ~ 295.9 eV (Li et al. 2020). The percentage of atoms occupied by each chemical state of the carbon atom is summarized in Table S3. The O 1 s spectral decomposition (Fig. S6b) identified three oxygen configurations: quinone-type C=O (~ 531.5 eV), carboxylate O=C–O (~ 532.1 eV), and ether-type C–O (~ 533.5 eV) (Zhang et al. 2021). Table S4 shows that the increase in pyrolysis temperature leads to the escape of some oxygen functional groups from the sample, which results in a decrease in the oxygen content. While the O/C atomic ratios remained relatively constant across samples (~ 0.075 ± 0.005), significant variations in N/C ratios from 0.037 to 0.33 occurred, and it is expected that nitrogen species are directly related to catalytic oxidation efficiency (Table S5).

High-resolution N 1 s spectra (Fig. 2f) resolved four nitrogen species assigned to pyridine N (Pyri-N, ~ 398.4 eV), pyrrole N (Pyrr-N, ~ 400.1 eV), graphite N (Grap-N, ~ 401.0 eV), and oxidized N (Oxid-N, ~ 404.3 eV), respectively (Chen et al. 2020). It's worth noting that CGNrC-T catalysts exhibited a systematic 3 ~ 4 eV binding energy downshift compared to CGC-700, indicative of enhanced electron density at nitrogen sites arising from structural defects. This finding aligns with the Raman-derived defect density trends (Fig. 2c), confirming the activation-induced generation of catalytically active defect sites. The total nitrogen content decreased drastically from 23.33 to 6.97 at.% with increasing pyrolysis temperature from 500 to 900 ℃, which is consistent with the FT-IR observations of diminishing C≡N/C=N signals (Fig. 2d). As displayed in Fig. 2g and Table S6, an increase in pyrolysis temperature leads to the conversion of Pyri-N to the more thermally stable Grap-N (≥ 40% at 900 ℃). Previous studies have shown that the lone electron pair on the Pyri-N could optimize the surface electronic structure of the carbon catalyst and provide basic sites, which can enhance the oxidation–reduction reaction (Zhang et al. 2025).

The adsorption and dissociation of H_2S mainly depend on the number and strength of basic sites on the catalyst surface. As illustrated in Fig. 2h, CO_2-TPD profiles of CGC-700 and CGNrC-700 revealed three distinct CO_2 desorption peaks within the 350–800 °C range, corresponding to weak, medium, and strong basic sites. It can be seen that activation treatment and N doping induced both moderate and strong basic sites that gradually shifted to higher desorption temperatures and had a

larger peak area, indicating the formation of more and stronger basic sites, favoring the adsorption and dissociation of H_2S molecules (Yuan et al. 2024). Similarly, O_2-TPD analysis was performed to understand the nature of oxygen species on the catalyst. CGNrC-700 exhibited higher O_2 desorption temperatures (Fig. 2i), suggesting a stronger interaction between CGNrC-700 and O_2 (Xiong et al. 2024).

Based on the aforementioned series of characterization analyses, the CGNC-700 catalyst prepared through a synergistic strategy of simple chemical activation and nitrogen doping, followed by pyrolysis at 700 °C, demonstrates significant structural advantages. This material possesses both a great specific surface area (787.8 m^2/g, Fig. 2e) and substantial nitrogen content (17.33 at.%, Fig. 2f) while simultaneously generating abundant lattice defect density ($n_D = 3.52 \times 10^{11}$, Table S1) and more and stronger basic sites. These structural characteristics can enhance reactant mass transfer efficiency, promote the adsorption of reactant molecules and oxygen molecule activation, and regulate product selectivity. Consequently, the CGNC-700 catalyst is anticipated to exhibit superior performance in the H_2S-SCO reaction.

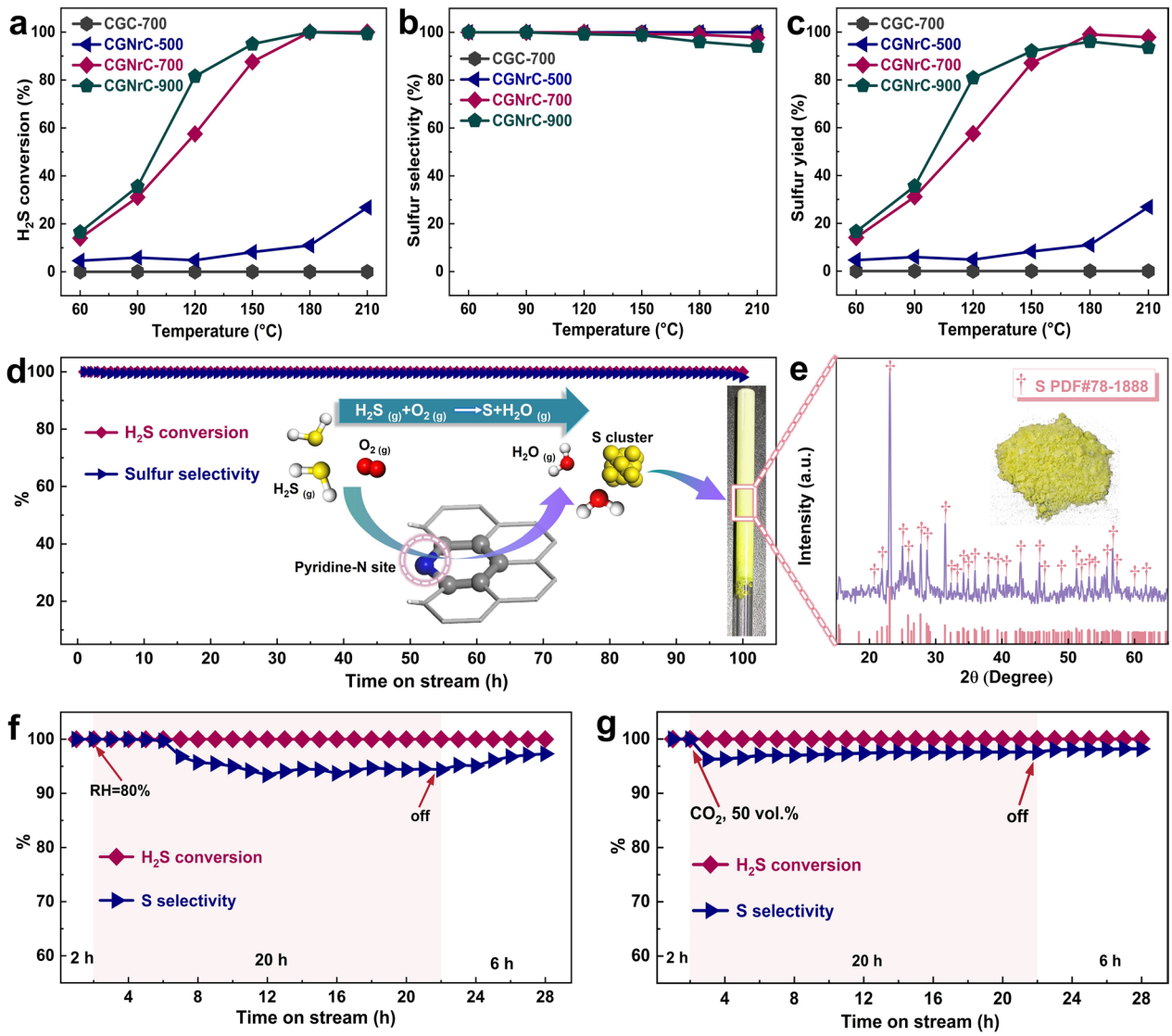

Fig. 3 Preparation of nitrogen-rich carbon catalysts for H_2S-SCO performance testing. **a** H_2S conversion, **b** Sulfur selectivity, and **c** Sulfur yield of all samples (reaction conditions: T = 60–210 ℃, WHSV = 60,000 mL/h/g, $C_{O_2}/C_{H_2S} = 0.5$). **d** Durability test of CGNrC-700 for H_2S-SCO (reaction conditions: T = 180 ℃, WHSV = 60,000 mL/h/g, $C_{O_2}/C_{H_2S} = 0.5$). **e** Comparison of product S with the S_8 standard card. **f**, **g** Effect of CO_2 and H_2O content on the desulfurization performance of CGNrC-700 (reaction conditions: T = 180 ℃, WHSV = 60,000 mL/h/g, $C_{O_2}/C_{H_2S} = 0.5$).

3.2 Catalysts performance

To evaluate the H_2S-SCO activity of all samples, performance tests were carried out in a fixed-bed reactor at atmospheric pressure. H_2S-SCO activities of all synthesized materials were evaluated under controlled conditions (Fig. 3a, c, d). CGC-700 exhibited negligible H_2S elimination capacity (< 1%), attributable to its insufficient SSA (26.7 m^2/g, Fig. 2e) and nitrogen content (3.33 at.%, Fig. 2f). The CGNrC-T series demonstrated a characteristic volcanic trend in catalytic performance with increasing reaction temperature. Specifically, despite its elevated nitrogen content, CGNrC-500 displayed suboptimal H_2S conversion efficiency due to limited SSA (21.3 m^2/g, Fig. 2e). While CGNrC-900 achieved enhanced catalytic oxidation efficiency, its sulfur selectivity exhibited a sharp decline (≥ 180 °C), owing to nitrogen content depletion during high-temperature pyrolysis (6.97 at.%, Fig. 2f). CGNrC-700 emerged as the optimal candidate, achieving complete H_2S conversion (100%) with near-unity sulfur selectivity (~ 99%) under identical reaction conditions. This exceptional performance originates from the synergistic integration of three critical structural advantages: (1) hierarchically porous architecture facilitating rapid mass transfer, (2) abundant nitrogen dopants enabling efficient oxygen activation, and (3) defect-rich carbon matrix providing substantial active sites. Furthermore, practical considerations, including energy consumption (avoiding > 700 °C pyrolysis) and environmental sustainability (minimizing SO_2 byproduct formation), reinforce the selection of CGNrC-700 as the preferred catalyst for subsequent performance evaluation and mechanistic investigations.

Long-term stability testing is a crucial indicator for evaluating the viability of catalysts in industrial applications. As shown in Fig. 3d, the H_2S conversion remained constant at 100% at 180 ℃ through 100 h of continuous operation, and a slight decrease in sulfur selectivity (~ 99%) was observed, attributed to the overoxidation of a small portion of the sulfur products and H_2S to SO_2. Additionally, the sulfur selectivity was tested at high oxygen concentrations when the O_2 concentration was eight times that of H_2S. As illustrated in Fig. S7, CGNrC-700 achieved simultaneous 100% H_2S conversion and 96% sulfur selectivity over 20 h of continuous operation, demonstrating that excellent S selectivity is essential in this practical application. The effect of WHSV on the catalyst activity of CGNrC-700 was studied when the WHSV was increased from 30,000 mL/h/g to 120,000 mL/h/g the H_2S conversion decreased from 100% to about 87% due to the shortened contact time between the feed gas and the catalyst (Fig. S8a), while the sulfur selectivity of the catalyst was maintained at 99% regardless of WHSV variations (Fig. S8b). As shown in Fig.S9, the CGNrC-700 effectively converts H_2S to elemental S, even at high concentrations of H_2S (0.5 vol.%). To verify the purity of the oxidation products, the collected sulfur was subjected to XRD analysis (Fig. 3e), which showed that the sulfur obtained was of high purity. As shown in Table S7, the nitrogen-rich carbon catalysts synthesized in this paper have a wide range of raw materials, low cost, and near 100% sulfur selectivity at high WHSV (60,000 mL/h/g) compared to previously reported carbon-based and metal-oxide catalysts.

To assess the practical viability of the optimal catalyst CGNrC-700, it was subjected to H_2S-SCO in high humidity (RH = 80%) and ultra-high CO_2 concentration (50 vol.%) environments, respectively. As displayed in Fig. 3f, the effect of high steam content on H_2S conversion was negligible, with the H_2S conversion remaining at 100% and 90% sulfur selectivity after 20 h at 180 ℃. Remarkably, the sulfur selectivity gradually recovered to 97.2% after water vapor cessation, indicating that the catalyst has outstanding water resistance. In CO_2-rich atmospheres (Fig. 3g), the tolerance of CGNrC-700 to impurity gases was investigated by passing CO_2 into the gas mixture; it achieved nearly 100% conversion with 97.4% sulfur selectivity within 20 h. The reduction in selectivity is because high concentrations of CO_2 can act as a weak oxidant, oxidizing elemental sulfur to SO_2 or sulfates (Wang et al. 2024a, b), confirming the excellent CO_2 resistance of the catalysts. The above results indicate that the coffee grounds-derived nitrogen-rich carbon catalyst prepared in this paper possesses satisfactory catalytic oxidation activity even under harsh reaction conditions, which proves its infinite potential for practical applications.

3.3 Regeneration of the spent catalyst

The renewability of a spent catalyst is one of the key factors in evaluating the value of catalyst application because it not only avoids secondary pollution caused by solid waste but also greatly reduces cost and saves resources. The CGNrC-700 catalyst has been previously tested for catalytic oxidation for up to 100 h at very high WSHV (60,000 mL/h/g), which showed no significant reduction in catalytic activity (Fig. 3d). When WSHV increases to 90,000 mL/h/g, the reaction rate is accelerated and the resulting product sulfur cannot be transferred in time, and therefore the H_2S conversion declined to ~ 90% after 35 h (Fig. 4a). From elemental mapping images (Fig. 4b) and EDS spectra (Fig. S10), S elements significantly increased and were uniformly distributed on the surface of the used catalyst (CGNrC-700-S), covering most of the N-active sites, which leads to lower H_2S conversion. The XRD analysis showed that the S species on the surface of CGNrC-700-S mainly existed in the form of crystalline

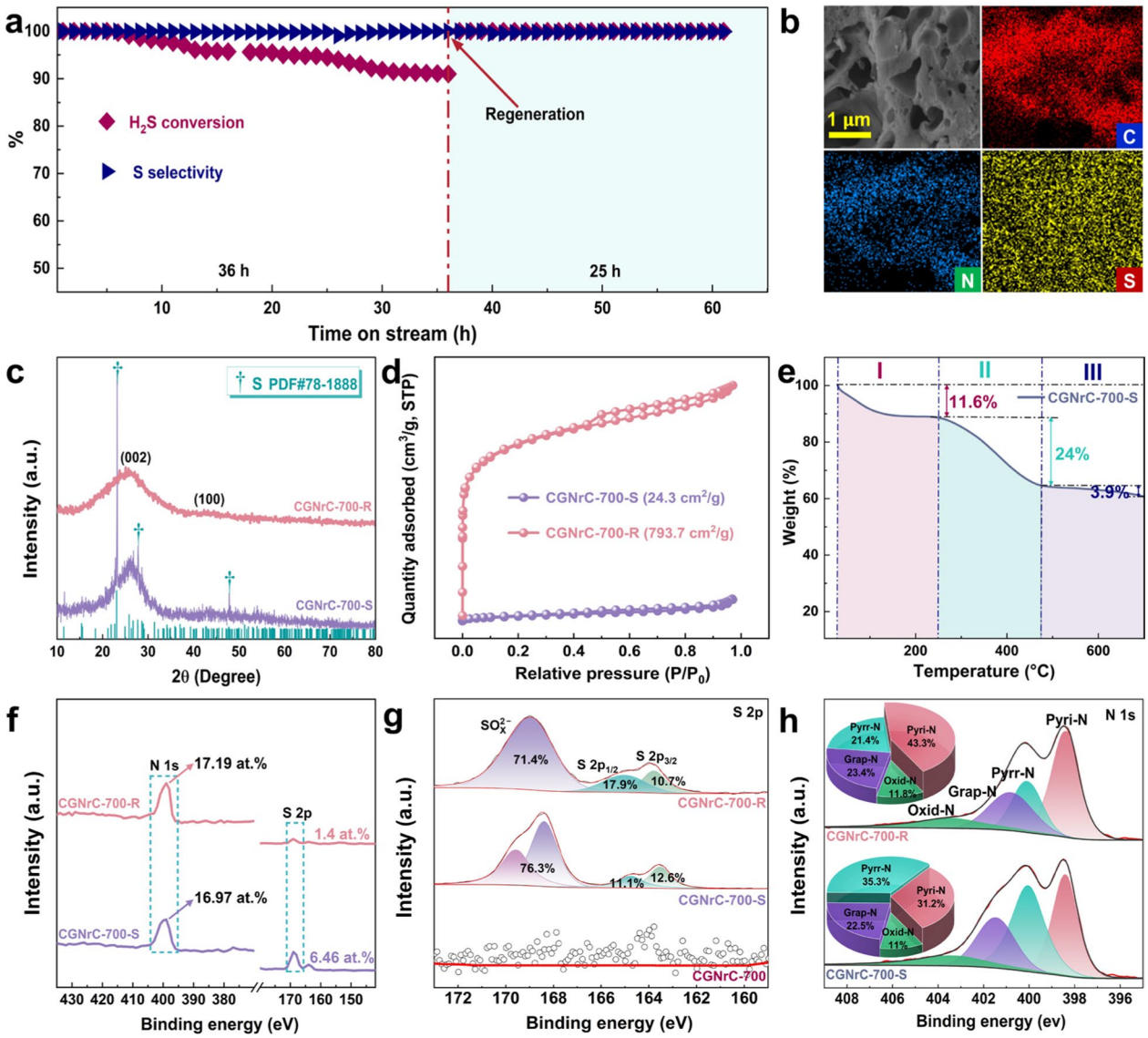

Fig. 4 **a** Explored the catalytic performance of CGNrC-700-R (reaction conditions: WHSV = 90,000 mL/h/g, T = 180 ℃, $C_{O_2}/C_{H_2S} = 0.5$). **b** EDS mapping images showing the elemental distribution of C, N, and S in the CGNrC-700-S. **c** XRD patterns and **d** N_2 adsorption–desorption isotherms of spent and regenerated catalysts. **e** TG analysis of CGNrC-700-S. **f** The XPS survey spectra of CGNrC-700-S and CGNrC-700-R. **g** High-resolution S 2p XPS spectra of CGNrC-700, CGNrC-700-S, and CGNrC-700-R. **h** High-resolution N 1 s XPS spectra of CGNrC-700-S and CGNrC-700-R

sulfur element (Fig. 4c) and would occupy the pore channels of the catalyst, leading to a reduction in SSA (24.3 m^2/g) (Fig. 4d). As shown in Figs. S11a and 11b, the reticulated pore structure channels of the CGNrC-700-S catalyst were blocked to form a block structure. In the FT-IR spectra (Fig. S12), only a significant reduction in the intensity of the C≡N stretch (2140 cm^{-1}) was observed, and the peak positions and intensities of CGNrC-700-S were essentially unchanged, suggesting partial nitrogen functionality loss without chemical structure degradation. According to the TG curve of CGNrC-700-S (Fig. 4e), a weight loss of 24% occurs at > 400 °C under an N_2 atmosphere, which is attributed to the sublimation of elemental sulfur. Based on this, we designed hot water washing and a 500 ℃ heat sweep, removing most of the sulfur to restore the catalytic activity of the spent catalyst. After regeneration by hot water washing and N_2 thermal sweeping, most elemental sulfur and sulfate accumulated on the catalyst surface were removed. The XPS analysis showed that the S content in CGNrC-700-R decreased from 6.46 to 1.4 at.%, while, the N content increased from 16.97 to 17.19 at.% compared to CGNrC-700-S (Fig. 4f).

As shown in Fig. 4g, the high-resolution S 2p XPS spectra of CGNrC-700-S were deconvoluted into four peaks, including peaks at approximately 169.7 eV (S 2p1/2) and 168.5 eV (S 2p3/2) signal assigned to elemental sulfur, as well as 164.8 eV and 163.5 eV, which were assigned to SO_x^{2-} (Grieger et al. 2020). Furthermore, in the high-resolution N 1 s spectra (Fig. 4h), the change in total N content in fresh and spent catalysts was negligible. However, the content of the Pyri-N dropped from 8.11 to 5.29 at.%. After regeneration, the Pyri-N content recovered to 7.45 at.%. As shown in Figs. 4d and S13, the blocked pore channels of CGNrC-700-S were released after the regeneration treatment, and the SSA was restored to 793.7 m^2/g. The revival of Pyri-N active sites and SSA is expected to contribute to enhanced catalytic oxidation of H_2S over the CGNrC-700-R catalyst. The experimental results (Fig. 4a) demonstrated that the catalytic activity of the CGNrC-700-S catalyst for H_2S was restored after regeneration, showing that the catalyst is structurally stable and recyclable.

3.4 Mechanism insights

It is reported that the Lewis basic site from the graphite edge position of Pyri-N is considered to be the active site for various catalytic reactions, including the catalytic oxidation reaction (Liu et al. 2025). We demonstrated the synthesis of a nitrogen-rich carbon catalyst with abundant defect sites and high nitrogen content through various characterization techniques (e.g., Raman, XPS, TEM, CO_2-TPD). The previous research demonstrated that the carbon adjacent to Pyri-N is the best adsorption site for H_2S and O_2 (Yang et al. 2024). However, the best active site among the carbon structures on the left and right sides of the pyridine nitrogen remains unstudied. Hence, we constructed a model of nitrogen-rich carbon-containing defects and active nitrogen sites (Fig. S14) and revealed the effect of doped N heteroatoms on the surface electrostatic potential (ESP) of the carbon framework calculated by DFT. On an optimized nitrogen-rich carbon model, the electronegativity of Pyri-N is much larger than that of neighboring carbon, leading to charge transfer between carbon and nitrogen (Fig. 5b). Combined with the properties of reactant molecules, it was hypothesized that the carbon sites near Pyri-N were identified as the optimal active sites for the adsorption of H_2S and O_2. Furthermore, the superior H_2S catalytic oxidation performance of the nitrogen-rich carbon catalyst can also be understood in terms of the frontier orbital energy gap (the difference between the LUMO and HOMO). As depicted in Fig. S15, compared with previous studies (Xue et al. 2024), the CGNrC-700 catalyst exhibits a narrow energy gap (1.73 eV) with excellent charge transfer properties, which facilitates the transfer of electrons from H_2S to the LUMO orbitals of the catalyst, thus promoting reactivity for H_2S conversion (Adio et al. 2020). Finally, adsorption energies of H_2S and O_2 at two adjacent carbon sites near Pyri-N were calculated (Fig. 5a and Fig. S16). The adsorption energies of O_2 at both carbon sites adjacent to Pyri-N were −1.28 eV. The adsorption energy of H_2S at the Pyri-N-C-C-H_2S (−0.11 eV) site was higher than that at the Pyri-N-C-H-H_2S site (−0.06 eV), demonstrating that the carbon site bonded to two carbons adjacent to Pyri-N is the optimal adsorption site for H_2S.

We performed DFT calculations to elucidate further the process and energy changes of H_2S-SCO over the CGNrC-700 catalyst. As displayed in Fig. 5c, the thermodynamic analysis of adsorption behavior reveals distinct characteristics between O_2 and H_2S on the catalyst surface. The calculated adsorption free energy (ΔG) values of −1.63 eV for O_2 and 0.22 eV for H_2S indicate a significant difference in their interaction mechanisms. The strongly negative ΔG value confirms the spontaneous chemisorption of O_2 molecules through chemical bond formation with active sites. In contrast, the slightly positive ΔG value for H_2S adsorption suggests a thermodynamically unfavorable process under standard conditions. It may be attributed to the competitive adsorption mechanism, where O_2 molecules preferentially occupy the most active sites as strong adsorbates. Notably, the catalytic oxidation of H_2S in this study was conducted under moderate thermal conditions (180 °C), which provides sufficient activation energy to overcome the initial adsorption barrier for H_2S. This thermal activation facilitates the formation of key reaction intermediates. These metastable intermediates subsequently undergo sequential reactions with incoming O_2 and H_2S molecules. The reaction pathway for forming the first sulfur atom with a ΔG value of −3.27 eV indicates a highly exothermic transformation process. The final reaction stage involves the conversion of the intermediate from the previous reaction with H_2S to form the second sulfur atom with an even more negative ΔG value of −4.63 eV. This substantial energy release drives the reaction toward complete sulfur production, confirming the thermodynamic favorability of the overall catalytic cycle. The stepwise decrease in free energy values throughout the reaction pathway (−1.63 eV → −3.27 eV → −4.63 eV) demonstrates an efficient energy cascade mechanism, where each successive reaction stage becomes progressively more thermodynamically favorable, ultimately ensuring high conversion efficiency to elemental sulfur.

Based on the above theoretical findings, we proposed a possible reaction mechanism to explain our observed results (Fig. 5d). It is widely recognized that H_2S-SCO over carbon-based catalysts follows

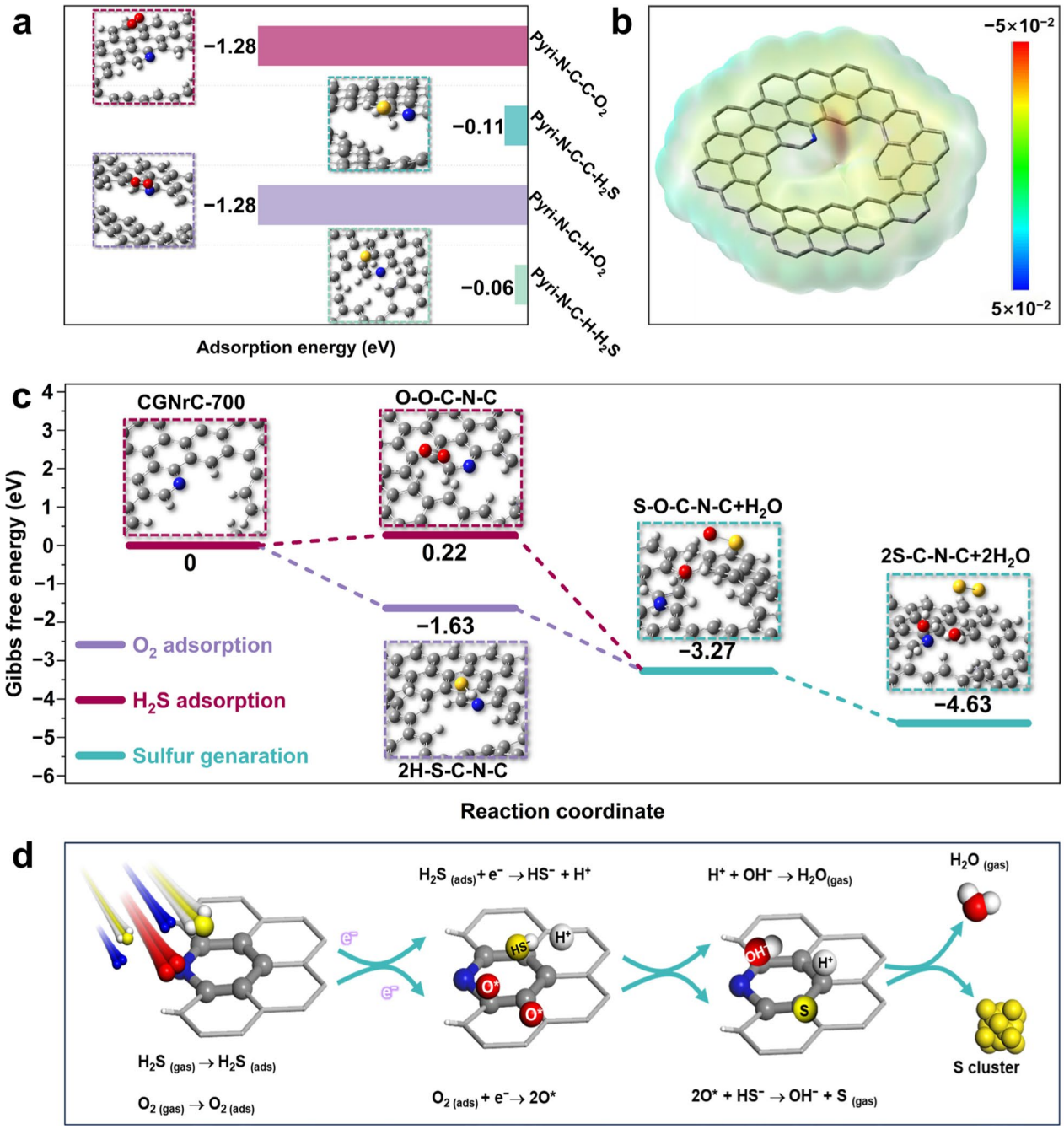

Fig. 5 **a** Adsorption energies of H_2S and O_2 molecules on different carbon sites. **b** Surface electrostatic potential distribution over the CGNrC-700 catalyst. **c** Gibbs free energy spectrum of H_2S-SCO over the CGNrC-700 catalyst. **d** Possible reaction mechanistic diagram of H_2S-SCO over CGNrC-700 catalyst surface

the Langmuir–Hinshelwood mechanism (Liu et al. 2024). Thus, the H_2S-SCO on CGNrC-700 can be categorized into three stages. The first stage is attributed to the charge transfer on the catalyst, promoting the adsorption of H_2S and O_2. The second stage is the dissociation of H_2S interacting with the basic sites of HS^-, N-doping results in the formation of abundant structural defect sites on the catalyst, which promotes charge redistribution to activate the O_2 molecules. The final stage corresponds to the reaction of HS^- and the activated oxygen molecule to generate elemental

sulfur and gaseous water molecules. The generated S may be oxidized by excess superoxide radicals to SO_2 and sulfates. The products, sulfur and sulfates, accumulate in the catalyst pore channels and cover the active sites on the catalyst surface, leading to catalyst deactivation.

4 Conclusion

In conclusion, we have demonstrated a feasible, sustainable, and cost-efficient strategy for synthesizing a nitrogen-rich carbon catalyst with exceptionally high nitrogen content. Coffee grounds and MCA were utilized as carbon and nitrogen sources, respectively, through hydrothermal treatment and controlled pyrolysis. We successfully developed the CGNrC-700 catalyst. Experimental results demonstrated prominent catalytic oxidation performance and remarkable stability with 100% H_2S conversion and 99% sulfur selectivity over continuous operation for up to 100 h. Moreover, the catalyst maintained robust catalytic activity under harsh reaction conditions, including high steam (RH = 80%) and elevated CO_2 concentration (50 vol.%). Combined experimental and DFT theoretical simulations reveal the origin of such high catalyst performance and propose the H_2S-SCO reaction pathway. Benefiting from the unique textural properties, the nitrogen-rich carbon catalysts derived from coffee grounds are promising for various sulfur-containing industrial off-gases for H_2S-SCO, providing new perspectives and a focus for green and sustainable resource utilization.

Supplementary Information

The online version contains supplementary material available at https://doi.org/10.1007/s42773-025-00541-4.

Supplementary material 1.

Acknowledgements
Not applicable.

Author contributions
Fei Zhao: material preparation, data collection, analysis and writing-original draft; Zibin Pan: Performed the DFT theoretical calculations; Shuo Cui and Fang Wang assist in analyzing data and discussions; Jiayu Feng: designed the study, revised the paper and provided financial support; Lijuan Jia and Ping Ning: supervision, funding. All authors read and approved the final manuscript.

Funding
This research leading to these results received funding from the Yunnan Fundamental Research Projects (No. 202401AU070028), the National Natural Science Foundation of China (No. 52300140 and 22476171).

Data availability
Data will be made available on request.

Declarations

Competing interests
The authors have no relevant financial or non-financial interests to disclose.

Author details
[1]School of Chemistry and Environment, Yunnan Minzu University, Kunming 650504, Yunnan, People's Republic of China. [2]Faculty of Environmental Science and Engineering, Kunming University of Science and Technology, Kunming 650500, Yunnan, People's Republic of China.

Received: 25 April 2025 Revised: 20 October 2025 Accepted: 28 October 2025
Published online: 31 January 2026

References

Adio SO, Ganiyu SA, Usman M, Abdulazeez I, Alhooshani K (2020) Facile and efficient nitrogen modified porous carbon derived from sugarcane bagasse for CO_2 capture: experimental and DFT investigation of nitrogen atoms on carbon frameworks. Chem Eng J 382:122964. https://doi.org/10.1016/j.cej.2019.122964

Battista F, Barampouti EM, Mai S, Bolzonella D, Malamis D, Moustakas K, Loizidou M (2020) Added-value molecules recovery and biofuels production from spent coffee grounds. Renew Sustain Energy Rev 131:110007. https://doi.org/10.1016/j.rser.2020.110007

Brazhnyk DV, Zaitsev YP, Bacherikova IV, Zazhigalov VA, Stoch J, Kowal A (2007) Oxidation of H_2S on activated carbon KAU and influence of the surface state. Appl Catal B Environ 70(1):557–566. https://doi.org/10.1016/j.apcatb.2005.12.028

Chan YH, Lock SSM, Wong MK, Yiin CL, Loy ACM, Cheah KW, Chai SYW, Li C, How BS, Chin BLF, Chan ZP, Lam SS (2022) A state-of-the-art review on capture and separation of hazardous hydrogen sulfide (H_2S): recent advances, challenges and outlook. Environ Pollut 314:120219. https://doi.org/10.1016/j.envpol.2022.120219

Chen F, Wu X-L, Yang L, Chen C, Lin H, Chen J (2020) Efficient degradation and mineralization of antibiotics via heterogeneous activation of peroxymonosulfate by using graphene supported single-atom Cu catalyst. Chem Eng J 394:124904. https://doi.org/10.1016/j.cej.2020.124904

Cychosz KA, Thommes M (2018) Progress in the physisorption characterization of nanoporous gas storage materials. Engineering 4(4):559–566. https://doi.org/10.1016/j.eng.2018.06.001

de Rink R, Klok JBM, van Heeringen GJ, Keesman KJ, Janssen AJH, ter Heijne A, Buisman CJN (2020) Biologically enhanced hydrogen sulfide absorption from sour gas under haloalkaline conditions. J Hazard Mater 383:121104. https://doi.org/10.1016/j.jhazmat.2019.121104

Feng J, Jia L, Wang F, Sun X, Ning P, Wang C, Li Y, Li K (2023) Urea-modified Cu-based materials: highly efficient and support-free adsorbents for removal of H_2S in an anaerobic and dry environment. Chem Eng J 451:138815. https://doi.org/10.1016/j.cej.2022.138815

Franca AS, Oliveira LS (2022) Potential uses of spent coffee grounds in the food industry. Foods 11(14):2064. https://doi.org/10.3390/foods11142064

Grieger S, Szydłowska BM, Rao VJ, Steinmann E, Dodds M, Gholamvand Z, Duesberg GS, Zaumseil J, Backes C (2020) Site-selective oxidation of monolayered liquid-exfoliated WS_2 by shielding the basal plane through adsorption of a facial amphiphile. Angew Chem Int Ed Engl 59(33):13785–13792. https://doi.org/10.1002/anie.202005730

He R, Xia F-F, Bai Y, Wang J, Shen D-S (2012) Mechanism of H_2S removal during landfill stabilization in waste biocover soil, an alterative landfill cover. J Hazard Mater 217–218:67–75. https://doi.org/10.1016/j.jhazmat.2012.02.061

Kan X, Chen X, Chen W, Mi J, Zhang J-Y, Liu F, Zheng A, Huang K, Shen L, Au C, Jiang L (2019) Nitrogen-decorated, ordered mesoporous carbon spheres as high-efficient catalysts for selective capture and oxidation of H_2S. ACS Sustain Chem Eng 7(8):7609–7618. https://doi.org/10.1021/acssuschemeng.8b05852

Khabazipour M, Anbia M (2019) Removal of hydrogen sulfide from gas streams using porous materials: a review. Ind Eng Chem Res 58(49):22133–22164. https://doi.org/10.1021/acs.iecr.9b03800

Kim M-J, Choi SW, Kim H, Mun S, Lee KB (2020) Simple synthesis of spent coffee ground-based microporous carbons using K_2CO_3 as an activation agent and their application to CO_2 capture. Chem Eng J 397:125404. https://doi.org/10.1016/j.cej.2020.125404

Kourmentza C, Economou CN, Tsafrakidou P, Kornaros M (2018) Spent coffee grounds make much more than waste: exploring recent advances and future exploitation strategies for the valorization of an emerging food waste stream. J Clean Prod 172:980–992. https://doi.org/10.1016/j.jclepro.2017.10.088

Laksaci H, Khelifi A, Trari M, Addoun A (2017) Synthesis and characterization of microporous activated carbon from coffee grounds using potassium hydroxides. J Clean Prod. https://doi.org/10.1016/j.jclepro.2017.01.102

Lei G, Tong Y, Shen L, Liu F, Xiao Y, Lin W, Zhang Y, Au C, Jiang L (2020) Highly active and sulfur-resistant Fe–N4 sites in porous carbon nitride for the oxidation of H_2S into elemental sulfur. Small 16(42):2003904. https://doi.org/10.1002/smll.202003904

Li D, Ding L-X, Chen H, Wang S, Li Z, Zhu M, Wang H (2014) Novel nitrogen-rich porous carbon spheres as a high-performance anode material for lithium-ion batteries. J Mater Chem A 2(39):16617–16622. https://doi.org/10.1039/C4TA03281K

Li S, Gu Q, Cao N, Jiang Q, Xu C, Jiang C, Chen C, Pham-Huu C, Liu Y (2020) Defect enriched N-doped carbon nanoflakes as robust carbocatalysts for H_2S selective oxidation. J Mater Chem A 8(18):8892–8902. https://doi.org/10.1039/D0TA00212G

Li S, Fu H, Zhang X, Liu X, Tuci G, Giambastiani G, Pham-Huu C, Liu Y (2024) Hierarchically porous, N-defect enriched C-nanosheets boost the H_2S selective oxidation to elemental sulfur. Appl Catal B Environ 343:123505. https://doi.org/10.1016/j.apcatb.2023.123505

Liang S, Mi J, Liu F, Zheng Y, Xiao Y, Cao Y, Jiang L (2020) Efficient catalytic elimination of COS and H_2S by developing ordered mesoporous carbons with versatile base N sites via a calcination induced self-assembly route. Chem Eng Sci 221:115714. https://doi.org/10.1016/j.ces.2020.115714

Liu Y, Song C, Wang Y, Cao W, Lei Y, Feng Q, Chen Z, Liang S, Xu L, Jiang L (2020) Rational designed Co@N-doped carbon catalyst for high-efficient H_2S selective oxidation by regulating electronic structures. Chem Eng J 401:126038. https://doi.org/10.1016/j.cej.2020.126038

Liu X, Zhou Y, Wang C-L, Liu Y, Tao D-J (2022) Solvent-free self-assembly synthesis of N-doped ordered mesoporous carbons as effective and bifunctional materials for CO_2 capture and oxygen reduction reaction. Chem Eng J 427:130878. https://doi.org/10.1016/j.cej.2021.130878

Liu X, Shan L, Sun X, Wang T, Liu Z, Liu Y (2024) Reusable salt-template strategy for synthesis of porous nitrogen-rich carbon boosts H_2S selective oxidation. Green Energy Environ 9(12):1866–1877. https://doi.org/10.1016/j.gee.2024.01.005

Liu X, Zhai X, Zhao Y, Shan L, Liu Z, Liu Y (2025) Sulfur modified N-doped carbocatalysts promote the selectivity for H_2S selective oxidation. Appl Catal B Environ Energy 362:124717. https://doi.org/10.1016/j.apcatb.2024.124717

Martínez-Ahumada E, López-Olvera A, Jancik V, Sánchez-Bautista JE, González-Zamora E, Martis V, Williams DR, Ibarra IA (2020) MOF materials for the capture of highly toxic H_2S and SO_2. Organometallics 39(7):883–915. https://doi.org/10.1021/acs.organomet.9b00735

Meng F-N, Di X-P, Dong H-W, Zhang Y, Zhu C-L, Li C, Chen Y-J (2013) Ppb H_2S gas sensing characteristics of Cu_2O/CuO sub-microspheres at low-temperature. Sens Actuators B Chem 182:197–204. https://doi.org/10.1016/j.snb.2013.02.112

Pagett M, Teng KS, Sullivan G, Zhang W (2023) Reusing waste coffee grounds as electrode materials: recent advances and future opportunities (Global Challenges 1/2023). Glob Chall 7(1):2370011. https://doi.org/10.1002/gch2.202370011

Pan Z, Gao Q, Chen Z (2023) Removal of As(III) and As(V) from mine groundwater using bimetallic Fe/Cu nanoparticles. Process Saf Environ Prot 180:192–204. https://doi.org/10.1016/j.psep.2023.10.014

Phatyenchuen S, Pongthawornsakun B, Panpranot J, Praserthdam P (2018) Effect of transition metal dopants (M=Nb, La, Zr, and Y) on the M-TiO_2 supported V_2O_5 catalysts in the selective oxidation of H_2S to elemental sulfur. J Environ Chem Eng 6(5):5655–5661. https://doi.org/10.1016/j.jece.2018.08.066

Shah MS, Tsapatsis M, Siepmann JI (2017) Hydrogen sulfide capture: from absorption in polar liquids to oxide, zeolite, and metal-organic framework adsorbents and membranes. Chem Rev 117(14):9755–9803. https://doi.org/10.1021/acs.chemrev.7b00095

Wang H, Ding H, Wang Z, Zhu Y, Chen Z, Song B (2024a) Heteroatoms-doped mesoporous carbon nanosheets with dual diffusion pathways for highly efficient potassium ion storage. Small 20(27):2310908. https://doi.org/10.1002/smll.202310908

Wang Y, Liu Y, Wang L, Perumal S, Wang H, Ko H, Dong C-L, Zhang P, Wang S, Nga TTT, Kim YD, Ji Y, Zhao S, Kim J-H, Yee D-Y, Hwang Y, Zhang J, Kim MG, Lee H (2024b) Coupling photocatalytic CO_2 reduction and CH_3OH oxidation for selective dimethoxymethane production. Nat Commun 15(1):6047. https://doi.org/10.1038/s41467-024-49927-1

Xiong Y, Wang L, Ning P, Luo J, Li X, Yuan L, Xie Y, Ma Y, Wang X (2024) Constructing oxygen vacancy-enriched Fe_3O_4@MnO_2 core–shell nanoplates for highly efficient catalytic oxidation of H_2S in blast furnace gas. Sep Purif Technol 336:126234. https://doi.org/10.1016/j.seppur.2023.126234

Xu C, Gu Q, Li S, Ma J, Zhou Y, Zhang X, Jiang C, Pham-Huu C, Liu Y (2021a) Heteroatom-doped monolithic carbocatalysts with improved sulfur selectivity and impurity tolerance for H_2S selective oxidation. ACS Catal 11(14):8591–8604. https://doi.org/10.1021/acscatal.1c01252

Xu C, Chen J, Li S, Gu Q, Wang D, Jiang C, Liu Y (2021b) N-doped honeycomb-like porous carbon derived from biomass as an efficient carbocatalyst for H_2S selective oxidation. J Hazard Mater 403:123806. https://doi.org/10.1016/j.jhazmat.2020.123806

Xue N, Zhou H-Y, Han Y, Li M, Lu H-Y, Chen C-F (2024) A general supramolecular strategy for fabricating full-color-tunable thermally activated delayed fluorescence materials. Nat Commun 15(1):1425. https://doi.org/10.1038/s41467-024-45717-x

Yang C, Ye H, Byun J, Hou Y, Wang X (2020a) N-rich carbon catalysts with economic feasibility for the selective oxidation of hydrogen sulfide to sulfur. Environ Sci Technol 54(19):12621–12630. https://doi.org/10.1021/acs.est.0c02967

Yang C, Florent M, de Falco G, Fan H, Bandosz TJ (2020b) $ZnFe_2O_4$/activated carbon as a regenerable adsorbent for catalytic removal of H_2S from air at room temperature. Chem Eng J 394:124906. https://doi.org/10.1016/j.cej.2020.124906

Yang C, Wang Y, Liang M, Su Z, Liu X, Fan H, Bandosz TJ (2023) Towards improving H_2S catalytic oxidation on porous carbon materials at room temperature: a review of governing and influencing factors, recent advances, mechanisms and perspectives. Appl Catal B 323:122133. https://doi.org/10.1016/j.apcatb.2022.122133

Yang J, Cui S, Zhao F, Wang F, Feng J, Ning P, Jia L (2024) Waste to wealth: discarded cigarette butt-derived metal-free N-rich carbon catalysts for the selective catalytic oxidation of hydrogen sulfide to sulfur. Environ Sci Technol 58(45):20267–20276. https://doi.org/10.1021/acs.est.4c06461

Yuan L, Wang X, Li X, Wang J, Wang L, Xiong Y, Xiao Y, Ning P (2024) Activated-carbon-induced morphological and crystal transformation of α-FeOOH for efficient catalytic removal of hydrogen sulfide from blast furnace gas. Sep Purif Technol 340:126770. https://doi.org/10.1016/j.seppur.2024.126770

Zhang X, Tang Y, Qiao N, Li Y, Qu S, Hao Z (2015) Comprehensive study of H_2S selective catalytic oxidation on combined oxides derived from Mg/Al-$V_{10}O_{28}$ layered double hydroxides. Appl Catal B Environ 176–177:130–138. https://doi.org/10.1016/j.apcatb.2015.03.057

Zhang X, Xu C, Li S, Liu X, Liu Y (2021) N-doped porous carbocatalyst engineering via modulating the crystalline size of ZIF-8 for continuous H_2S selective oxidation. Appl Mater Today 25:101228. https://doi.org/10.1016/j.apmt.2021.101228

Zhang Z, Zhang F, Song Z, Zhang L (2025) Oxygen reduction reaction on pyridinic nitrogen-functionalized carbon: active site quantification and effects of Lewis basicity. ACS Catal 15(1):296–309. https://doi.org/10.1021/acscatal.4c05289

Zheng X, Li Y, Zhang L, Shen L, Xiao Y, Zhang Y, Au C, Jiang L (2019) Insight into the effect of morphology on catalytic performance of porous CeO_2 nanocrystals for H2S selective oxidation. Appl Catal B Environ 252:98–110. https://doi.org/10.1016/j.apcatb.2019.04.014

Zheng X, Li Y, Zheng Y, Shen L, Xiao Y, Cao Y, Zhang Y, Au C, Jiang L (2020) Highly efficient porous $Fe_xCe_{1-x}O_{2-\delta}$ with three-dimensional hierarchical nanoflower morphology for H_2S-selective oxidation. ACS Catal 10(7):3968–3983. https://doi.org/10.1021/acscatal.9b05486

Zheng X, Cai J, Zhao W, Liang S, Zheng Y, Cao Y, Shen L, Xiao Y, Jiang L (2021) Porous α-Fe_2O_3/SnO_2 nanoflower with enhanced sulfur selectivity and stability for H_2S selective oxidation. Chin Chem Lett 32(7):2143–2150. https://doi.org/10.1016/j.cclet.2020.11.017